



**HAL**  
open science

## **Ceramic Powder Bed Laser Sintering (CPBLS) on copper-doped hydroxyapatite: Creation of thin (5–50 $\mu\text{m}$ thick) consolidated ceramic patterns**

Tiphaine Bazin, François Rouzé-L'alzit, Alain Demourgues, Isabelle Julien, Sylvain Catros, Caroline Bertrand, Eric Champion, Thierry Cardinal, Manuel Gaudon

### **► To cite this version:**

Tiphaine Bazin, François Rouzé-L'alzit, Alain Demourgues, Isabelle Julien, Sylvain Catros, et al.. Ceramic Powder Bed Laser Sintering (CPBLS) on copper-doped hydroxyapatite: Creation of thin (5–50  $\mu\text{m}$  thick) consolidated ceramic patterns. *Ceramics International*, 2021, 47 (13), pp.18565-18574. 10.1016/j.ceramint.2021.03.182 . hal-03281974

**HAL Id: hal-03281974**

**<https://unilim.hal.science/hal-03281974v1>**

Submitted on 9 May 2023

**HAL** is a multi-disciplinary open access archive for the deposit and dissemination of scientific research documents, whether they are published or not. The documents may come from teaching and research institutions in France or abroad, or from public or private research centers.

L'archive ouverte pluridisciplinaire **HAL**, est destinée au dépôt et à la diffusion de documents scientifiques de niveau recherche, publiés ou non, émanant des établissements d'enseignement et de recherche français ou étrangers, des laboratoires publics ou privés.

# **Ceramic Powder Bed Laser Sintering (CPBLS) on copper-doped hydroxyapatite: creation of thin (5 – 50 micron thick) consolidated ceramic patterns.**

Tiphaine Bazin<sup>a,b</sup>, François Rouzé-l'Alzit<sup>a</sup>, Alain Demourgues<sup>a</sup>, I. Julien<sup>b</sup>, C. Bertrand<sup>a</sup>, S. Catros<sup>c</sup>, Thierry Cardinal<sup>a</sup>, Eric Champion<sup>b</sup> and Manuel Gaudon<sup>a,\*</sup>

*a Univ. Bordeaux, CNRS, Institut de Chimie de La Matière Condensée de Bordeaux, UMR 5026, F-33600, Pessac, France*

*b Univ. Limoges, CNRS, Institut de Recherche sur Les Céramiques, UMR 7315, F-87000, Limoges, France*

*c Univ. Bordeaux, INSERM, BioTis U1026, CHU Bordeaux, Oral Surgery Department, 33076 Bordeaux, France*

## **Abstract**

Implants made of ceramics, and more particularly of calcium phosphates (hydroxyapatite: HA, mainly), promoting intimate contact with natural bone are nowadays merging. Addition of copper ions in bio-ceramics is expected to increase the biological compatibilities of bone graft substitutes. Previous works have shown that copper-doped hydroxyapatite (Cu-doped HA) ceramics can be prepared by solid-state sintering between HA and CuO powder mixtures at about 1100°C; but, copper-substituted HA was found to be metastable leading to apatitic grains and Cu-rich grain boundaries during the sintering process. Ultra-rapid sintering is so needed. Selective laser sintering (SLS) is an additive manufacturing process that possesses the advantage to be based on ultra-fast sintering process under laser irradiation. SLS being used in literature for the application of laser on polymer-

ceramic or polymer-metal composites the proper term all along the paper is Ceramic Powder Bed Laser Sintering (CPBLS). To achieve densification of Cu-doped HA ceramics from CPBLS process, one should control the composition/morphology/structure of the powder bed as well as three other important CPBLS parameters: (i) the applied energy from the laser beam, (ii) the laser power and the laser scanning speed, (iii) the distance between two successive laser lines. In this paper, the impact of all the main CPBLS parameters controlling the sintering of dip-coated Cu-doped HA layers on glass substrates is carefully investigated. Possibility of the creation of thin consolidated Cu-doped HA ceramic patterns, using the ultra-fast CPBLS process, is finally shown.

**Keywords.** Laser Sintering ; Ceramic; Hydroxyapatite; Thin Films

## **1. Introduction**

Besides conventional shaping processes, the development of 3D printing has favoured the production of complex pieces/devices in small series while reducing production time since some steps such as the manufacture of moulds are no longer necessary. The evolution of digital modelling and simulation tools allows the production of complex shapes whether at the geometric or hierarchical level. Indeed, objects with cavities, inclusions or honeycomb-like structures can be easily printed [1-7]. Many additive manufacturing techniques have thus emerged depending on the type of material used and the intended application. All these techniques are based on the same manufacturing principle: the shaping of a three-dimensional part by a stack of successive layers, each of which undergoes a two-dimensional structuring. In the biomedical field, especially in bone reconstruction, additive manufacturing has grown considerably in recent years [8-13]. Indeed, it offers the possibility of reconstructing damaged areas thanks to the design of personalized parts with a complex architecture, adapted to the patient's morphology [14]. Implants made of ceramics, and more particularly of calcium

phosphates (hydroxyapatite: HA, mainly), promote intimate contact with natural bone. Their shaping by additive manufacturing is mainly done by stereolithography, which is the most widespread and popular technique today for designing ceramic parts [15-16]. This technique makes it possible to manufacture complex shaped parts with a resolution of the order of 10 microns via the laser light curing of a ceramic suspension. But after shaping, sintering (conventional conditions) is necessary in order to consolidate the final ceramic part, which can represent an important limitation for various applications. In another process: indirect selective laser sintering process, a polymer is typically used with the ceramic powder as binder. On hydroxyapatite compounds, most of the works are focused on the manufacture of HA-polymer composites in which the amount of HA constitutes a minor part. Among the biocompatible polymers used, mention may be made of polyetheretherketone (PEEK) [17, 18], polyamides [19, 20] or polycaprolactone (PCL) [21, 22]. Only few papers reported works on “direct selective laser sintering of bio-ceramics” (what is called herein CPBLS process), and less again on HA-based compounds. From CPBLS, 3D devices of complex shape can be sintered directly from a powder bed (coated using scrapers or rollers) or a powder film (produced by tape casting or dip coating), without additives. The selective laser sintering process consists of selectively sintering the particles of a powder bed (metal, ceramic, polymer, glass) using an infrared laser beam. The two main types of lasers used are the CO<sub>2</sub> laser with a radiation of 10.6 μm wavelength and the Nd: YAG laser, 1.06 μm wavelength. Irradiation of the powder by the laser beam, at a temperature below its melting point, thermally activates the diffusion of the atoms causing the formation of bridges at the interface between adjacent particles (local sintering phenomenon). Hence, direct laser sintering consists of consolidating the bed of powders by diffusion of the atoms like in the conventional solid-state route. In a recent study, Shuai *et al.* investigated the selective laser sintering of nano-sized hydroxyapatite particles: sintered parts built with 300 μm thick layers could be designed

using a laser beam with a diameter of 4  $\mu\text{m}$  and a power of 50 W. The low speeds used, ranging from 50 to 300  $\text{mm}\cdot\text{min}^{-1}$ , made it possible to increase the laser-material interaction time and therefore to promote the diffusion of atoms. In the two studies conducted by Shuai *et al.* [23, 24], the influences of energy density (2 - 5  $\text{J}\cdot\text{mm}^{-2}$ ) and beam power (between 2 and 10 W) on the sintering efficiency of HA nano-powder were studied. Besides the composition/morphology/structure of the powder, four very important laser parameters control the CPBLS process of ceramics as HA.

(i) *Influence of applied energy.* During the manufacturing, if the applied energy is too low, the consolidation between the particles and the different layers will be insufficient, causing the creation of pores and delamination of the layers. Increasing the energy applied increases the final density of the parts. A denser and more mechanically resistant structure is then obtained [25, 26]. However, at very high energies, the amplification of the thermal gradient induces greater stresses within the material, which can lead to the formation of cracks and curving phenomena [27]. Nevertheless, it has been proved that samples irradiated with the same energy density but with distinct power / speed pairs present a different microstructure affecting the density and the final mechanical properties of the part [28, 29]. The energy applied to a line ( $\text{J}\cdot\text{mm}^{-1}$ ) or to a volume ( $\text{J}\cdot\text{mm}^{-3}$ ) is actually proportional to the power of the laser beam and inversely proportional to the laser scanning speed. To take into account only the applied energy is then insufficient for a deep control of CPBLS process.

(ii) *Influence of laser power and laser scanning speed.* With increasing power and/or decreasing scanning speed, the transferred energy to the matter from the laser is increased [30-32]. Laser sintering is in particular more efficient at low speeds. Indeed, the decrease of the scanning speed increases the time of laser-matter interaction and therefore the energy absorbed by the powder bed is more homogeneous. Conversely, at too high scanning speeds, the laser / material interaction time becomes insufficient to consolidate properly the particles

[13, 33]. The laser power-speed couple must therefore be optimized as a function of the desired final properties [34, 35].

(iii) *Influence of the thickness of the powder bed.* The thickness of the powder bed (or layer) plays an essential role in the geometric precision and density of the final product. In fact, when the laser scans the bed of powder, the energy of the laser is absorbed by a thin layer of particles inducing a high temperature within the particles on the surface, as explained above. The lower the thermal conductivity of the material, the more difficult the heat generated during the laser-material interaction is to transfer to the bottom limit of the powder bed, especially for a thick layer. To ensure better consolidation of the 3D part, the thickness of the layer must be reduced so that the laser penetrates also a part of the previous one, thus promoting sintering between adjacent layers [26]. When the layers are thinner, the partial fusion of the particles is more homogeneous within the bed of powders which allows the improvement of the geometric precision, the reduction of the surface roughness and the increase of the relative density of the final piece [25, 26, 36, 37]. The sintering of thin layers also minimizes the temperature gradient and the volume shrinkage of the powder bed, thus reducing the stresses within the material and so crack appearing.

(iv) *Influence of the distance between 2 lased lines.* Influence of the distance between two lines on the microstructure of the sintered part is similar to that of the thickness of a layer: reducing the spacing between the beads improves geometric precision, decreases surface roughness and increases the rate of densification of the parts and therefore their mechanical resistance [35, 26, 31, 37]. In fact, the greater the distance between two lines, the more the successive sintered beads move apart, forming a part of high porosity. On the other hand, when the distance is short enough for the lines to overlap, the laser beam irradiates the current bead but also the previous one, partially. The matter transport, which then takes place between the adjacent lines, promotes their adhesion and the consolidation of the part. In addition, the

partial overlap of the beads makes it possible to compensate the Gaussian dispersion of the laser radiation intensities along the axis of the bead and the thermal conductivity profiles within the material which causes a temperature gradient which decreases from the centre to the outside of the lased line.

The combination of the appropriate parameters would *a priori* make it possible to modulate the final microstructure of the 3D part such as its geometric precision, its surface roughness and its porosity. However, improving one of these properties can sometimes come at the expense of another, so a compromise must be addressed depending on the application.

In this paper, in order to evaluate the impact of the four main laser parameters, which control the CPBLS process, we focused on dip-coating layers (from thin to thick films) of HA-based compounds dip-coated from ethanol suspension on glass substrates. Preliminary CPBLS tests were applied to HA thick films to roughly determine the set of appropriate laser parameters and the HA powder heat-treatment conditions. One can note that copper-doped compounds are studied since copper leads to control the absorptivity of the powder at the laser wavelength (essential parameter to convert efficiently laser energy into heat) and copper, known for its angiogenic properties, may improve the biological response of HA ceramics in view of their use as biomedical implants [38, 39].

## **2. Experimental**

### *2.1. HA Powder preparation*

Raw HA was synthesized by co-precipitation. The protocol consisted of adding, at a controlled rate and a constant pH (regulated thanks to ammonia:  $\text{NH}_4\text{OH}$ , Fisher Scientific), a phosphate solution (di-ammonium hydrogen-phosphate:  $(\text{NH}_4)_2\text{HPO}_4$ , Fisher Scientific) to a calcium solution (obtained from dissolution of calcium nitrate:  $\text{Ca}(\text{NO}_3)_2 \cdot 4\text{H}_2\text{O}$ , Sigma-Aldrich). The quantities of the reagents were calculated to obtain a molar ratio  $\text{Ca/P} = 10/6$ .

The synthesis conditions set were a pH=8.5 with a bath temperature maintained at 85°C. The synthesis was performed under argon gas flow during a maturation period to 5 hours. The as-prepared precipitate was then centrifuged and washed with distilled water before being dried in an oven at 100°C. The dried powder was calcined at 600°C for 1 h (10°C.min<sup>-1</sup> ramp) to remove reaction by-products such as nitrates. Next, a quantity of copper (II) oxide CuO (Alpha Aesar) was mixed to the HA powder to get a copper concentration of 5 mol%, *i.e.* to get the chemical composition formula Ca<sub>10</sub>Cu<sub>0.5</sub>(PO<sub>4</sub>)<sub>6</sub>(OH)<sub>1.5</sub>O<sub>0.5</sub>. The HA-CuO powder mixture was attrition milled to reduce particle size and further promote solid-state reaction. Attrition was performed in a 100 mL Teflon bowl in the presence of approximately 50 mL of distilled water, 1 wt% Darvan CN dispersant and 75 g yttrium-stabilized zirconia balls of 1 mm diameter. Attrition speed of 800 rpm was applied for 3 hours. The suspension was then oven dried at 100°C, and with the obtained powder, 10 mm diameter pellets were die pressed by applying a uniaxial pressure of 100 MPa. Finally, the pellets were calcined (ramp 10°C.min<sup>-1</sup>) for 1 hour at 1100°C to obtain a pure Cu-doped HA phase [40].

## 2.2. HA Film preparation

In order to study the impact of Cu-doped HA film thickness on laser sintering, controlled thickness layers were developed by the dip-coating technique. This method consists of immersing a substrate, a glass slide, in a ceramic suspension and removing it at a fixed speed to control the thickness of the deposit. The increase of withdrawal rate of the substrate leads to an increase of the wettability forces to the detriment of the gravity forces on the suspension and therefore makes it possible to increase the film thickness deposited on the glass substrate.

The ceramic suspension is produced by adding 30 wt% of Cu-doped HA powder functionalized with 2 wt% of dispersant (BeycoStat C213) to ethanol. The thin film is deposited at a withdrawal speed of 400 mm.min<sup>-1</sup>. At this speed, corresponding practically to



the maximum speed of the device, a film of a few microns thick ( $<5 \mu\text{m}$ ) is obtained. To increase the total thickness of the thin layer, several successive layers (2, 6 and 12) are deposited on the glass substrate. Between each deposition, the substrate is placed in an oven at  $100^\circ\text{C}$  for about 1 min to ensure the drying of the layer just deposited.

### *2.3. HA film laser sintering*

The CPBLS experiments have been conducted using a laser system especially designed according to the laboratory specifications by ES Laser (ES17-355). Laser is equipped with IPG Photonics ytterbium fiber laser (YLM-400-AC\*Y11) at a monochromatic wavelength of  $1.07 \mu\text{m}$ , and a galvanometric mirrors scanner (ScanLab - Hurry scan 20). This equipment has maximum and minimum operating power 400 W and 40 W, respectively. Its focal length was 199 mm and could be adjusted in  $100 \mu\text{m}$  increments. The spot size is  $50 \mu\text{m}$  and the maximum lased surface is  $75 \times 75 \text{ mm}^2$ .

Laser sintering machine was controlled by SamLight® software which allows the modulation of the laser power (as a % of maximum power), scanning speed (in  $\text{mm}\cdot\text{s}^{-1}$ ) and focal length (m). The required pattern was also directly drawn from software possibilities.

### *2.4. Characterization techniques*

X-ray diffraction patterns were recorded on a Philips X'Pert MPD apparatus equipped with a copper  $\text{K}_{\alpha 1}$  anticathode (40 kV, 40 mA). Diffraction patterns were collected from  $8$  to  $80^\circ$  in  $2\theta$  with a  $0.017^\circ$  step scan and a counting time of 59 s.

Chemical mapping using energy dispersive X-ray spectroscopy (EDS) in scanning transmission electron microscopy (STEM) was performed on a TEM equipped with a field emission gun: JEM 2100F (JEOL, 200 kV) coupled with energy X-ray spectrometer.

UV-Vis-NIR diffuse absorbance spectra were recorded at room temperature from 200 to 800 nm with a step of 1 nm and a band length of 2 nm on a Cary 17 spectrophotometer using an integration sphere. Halon polymer (ChemIndustry) was used as white reference for

the blank. A mathematic treatment of the obtained spectra allowed the determination of the  $L^*a^*b^*$  space colorimetric parameters, with L the luminosity,  $a^*$  the green to red axis and  $b^*$  the blue to yellow axis.

The morphology of the as-prepared particles was observed thanks to a Leica DMI 3000 M inverted microscope using a Leica SFL 100 diode enabling an excitation at 365 nm and the fluorescence collection recorded with a Leica MC 120 HD camera. Microscope objective N PLAN EPI 10 $\times$ , NA 0.25 was used. For microstructural analyses, SEM investigations were performed using a TESCAN Vega II SBH microscope or JEOL JSM-6700F. The film thickness was measured from SEM cross section views or by the Dektak 150 Surface Profiler (Veeco), allowing the plot of surface profiles thanks to a stylus with a tip radius of 12.5  $\mu\text{m}$  and a resolution of 0.8  $\mu\text{m}$ .

### **3. Results and discussion**

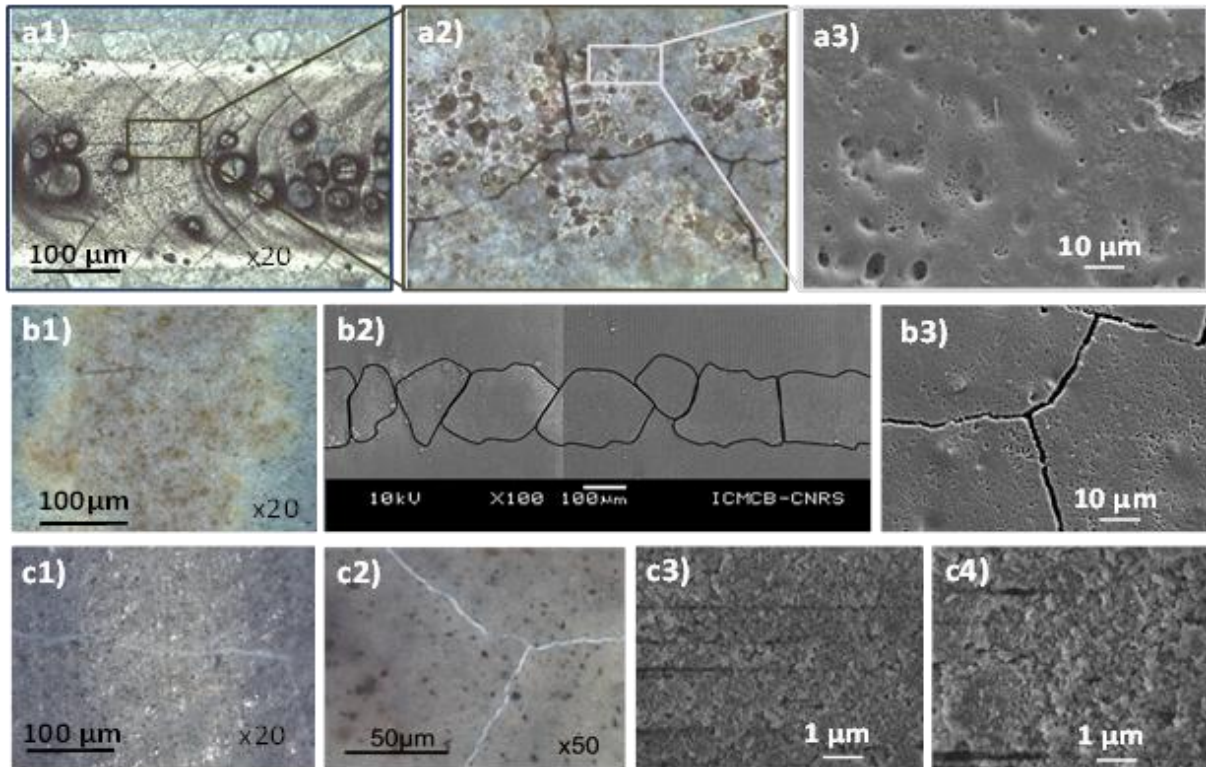
#### *3.1. First CPBLS experiments on thick films constituted by CuO – HA powder mixture*

The first series of sintering experiments by the CPBLS process were carried out on compacted pellets. Based on previous work in the literature showing the possibility to perform the selective laser sintering of a powder bed constituted mainly by a white matrix (zirconia) using a dispersion of carbon grains strongly absorbing at the laser wavelength [40, 41], we hoped to reproduce this effect. Since the CuO crystallites were black particles (and so hot-spots) dispersed into the white HA matrix, we chose to perform these first experiments on mixtures of HA powder (hydroxyapatite) and CuO powder (5 mol% CuO – 95 mol% HA) blended in an agate mortar.. Reactive sintering between copper oxide and HA was expected by localized heating of the copper oxide grains inducing  $\text{Cu}^{2+}$  cations diffusion within the surrounding HA crystals, hence leading to the appearance of the Cu-doped HA compound. Several rounds of irradiation were performed on the pellet surfaces, changing the power and

speed parameters of the laser. Based on the linear energy ( $\text{J}\cdot\text{m}^{-1}$ ) brought to the material by the laser (laser power / laser speed), the experiments can be grouped into three batches: low energy irradiations (series a), irradiations of intermediate linear energy (series b), irradiations of high linear energy (series c). Images from light microscopy (**Figure 1.a1, b1, c1, c2**) and scanning electron microscopy (**Figure 1.a2, a3, b2, b3, c3**) are grouped below. The high linear energies cause an excessively high temperature increase, with the formation of bubbles, characteristic of the fusion of the irradiated zones, associated with the presence of cracks.

The intermediate energies lead to a color change of the irradiated area with speckled appearance in optical microscopy (Figure 1.b1). The initially black CuO grains have reacted to the heat effect induced by laser beam, then turned as purple large areoles with the local diffusion into HA matrix. Hence, copper grains behaved like hot spots, leading to  $\text{Cu}^{2+}$  ions diffusion into HA matrix and the appearance of the purple coloration, which is associated with Cu-doped HA compounds. One of the solutions to solve this speckled appearance issue would be to pre-anneal the pellets in order to homogenize the copper distribution into the HA matrix. Figure 1.b3 shows that without this pre-treatment, only a partial sintering can be reached. Nonetheless, intermediate energy lasing seems adequate for the consolidation of the HA, Indeed, the zones lased under intermediate linear energy only present a porosity of about 20% (estimation by image processing) with a continuous network of particles having formed, with clearly visible inter necks on the SEM images, whereas the green film porosity was around 50-60%). However, despite several attempts to optimize both the chemical composition (CuO/HA concentration ratio) or power/speed of the laser, crack propagations could not be avoided. These cracks then form, all along the laser line (Figure 1.b2), a series of scales of around one hundred microns in diameter (in correlation with the diameter of the irradiation spot of 50 microns for a laser whose adjustment and focusing is perfect).

For the lowest linear energies the reactive sintering is not very advanced, no sintering neck is detectable, and the CuO grains are still present. Moreover, cracks are always detectable, especially in Figure 1.c2.



**Figure 1.** Optical images or SEM top views on CuO-HA thick films after CPBLS process applied with various energy ranges (a) high energy; b) intermediate energies and c) low energies

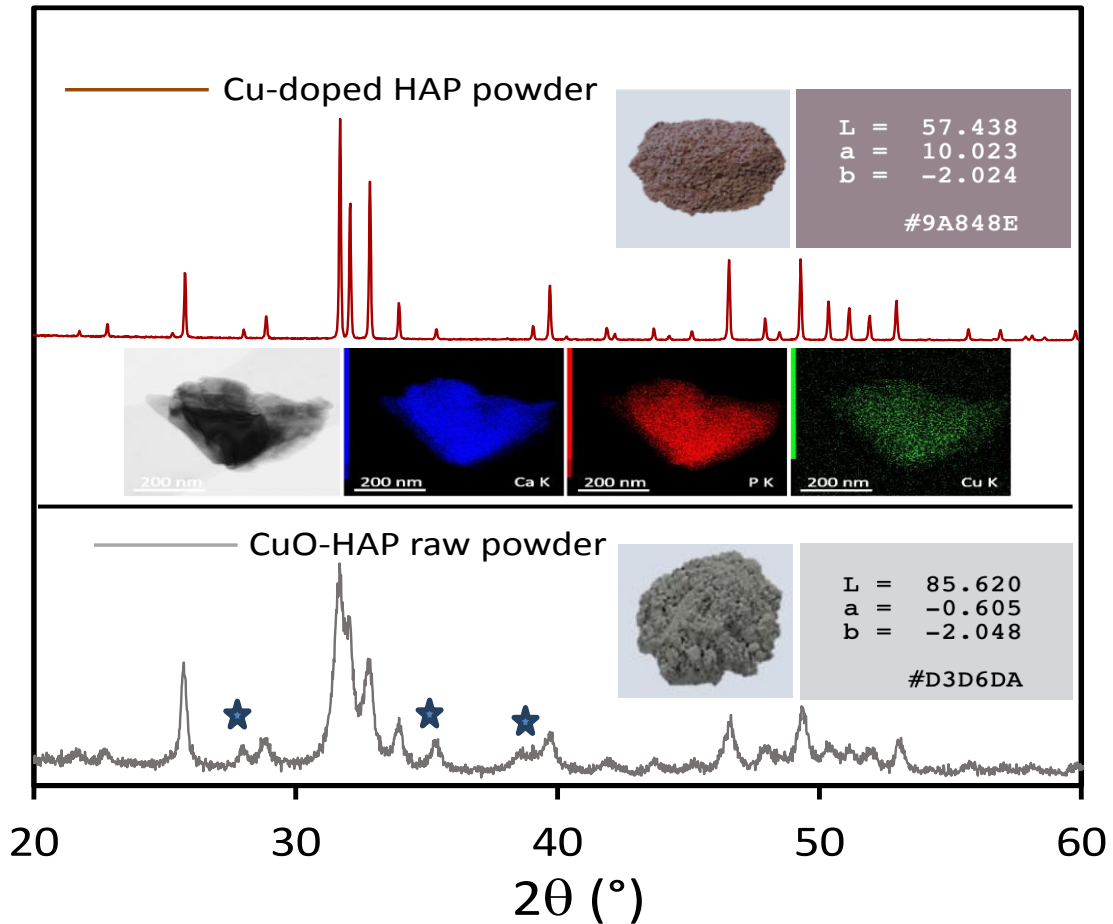
Thus, in the case of selective laser sintering, the reaction between HA and CuO cannot take place simultaneously with sintering, unlike by conventional sintering [40]. The inhomogeneity of heating between the black grains of CuO and the white hydroxyapatite leads even for the most adequate powers to the appearance of cracks while the distribution of copper is not yet homogeneous. The use of copper-doped HA as starting material on which reactive sintering has already been carried out seems mandatory. The target is to perform a preliminary homogeneous incorporation of the copper element into the matrix in order to

achieve the preparation of a monophasic Cu-doped HA pink powder (*i.e.* with copper being introduced with oxidation state + I) [38, 40, 41].

Furthermore, these experiments show that on compacted powder pellets, the appearance of cracks seems to be difficult to avoid and can constitute a major lock. To increase the chances of success in terms of densification without appearance of cracks under laser irradiation, experiments on thin layers, opening the possibility to tune the laser amplitude effect with the film thickness were carried out. Indeed, on the one hand, the thin layer deposition could give a more elastic character to HA ceramics and on the other hand, the adhesion with the substrate could limit the appearance of cracks.

The thermal pre-treatment was optimized by coupling structural (XRD), colorimetric (UV-visible-NIR spectroscopy) and chemical (EDS mapping) characterizations (**Figure 2**).

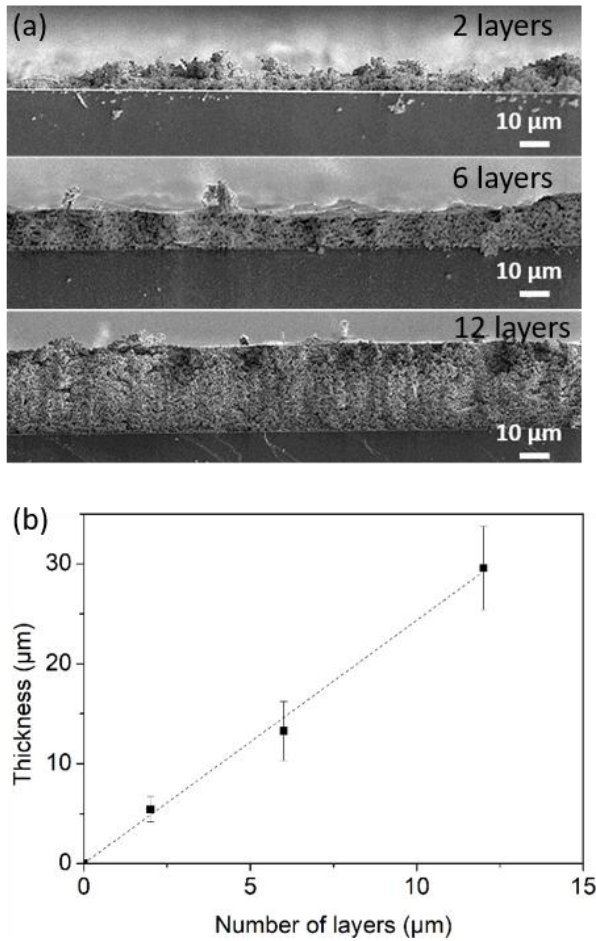
While the HA-CuO initial mixture (95 mol% - 5 mol%) exhibits broad HA peaks reflecting the nanometric character of the starting HA powder obtained by coprecipitation with addition of CuO peaks, the diffractograms obtained after annealing for 4 hours at 1100°C show the presence of a single phase of hydroxyapatite (Cu-doped HA). In addition, EDX maps show that the distribution of copper in the bulk of the HA grains is homogeneous. Finally, while the HA-CuO precursor mixtures exhibit a grey coloration (the HA matrix being a white compound and cupric oxide being black) the Cu-doped HA phase exhibits a pink coloration, characteristic of the incorporation of copper in the monovalent state of oxidation in insertion sites of the HAP structure [38, 40].



**Figure 2.** X-ray diffraction patterns of the CuO-HA raw powder mixture (bottom) and the Cu-doped HA powder (top) obtained after the annealing treatment at 1100°C (the star indicates the main CuO diffraction peak). Photograph and  $L^*$ ,  $a^*$ ,  $b^*$  colorimetric parameters associated to the raw mixture and the annealed powder. STEM EDS mapping showing the homogeneous cationic distribution (Ca, P, Cu) in the Cu-doped HA phase.


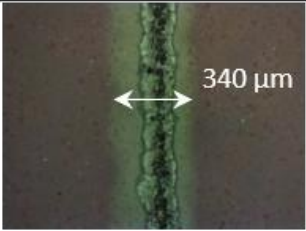
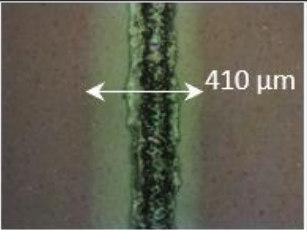


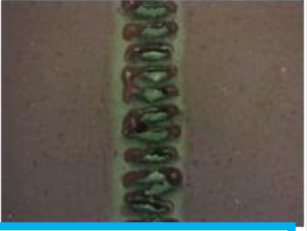

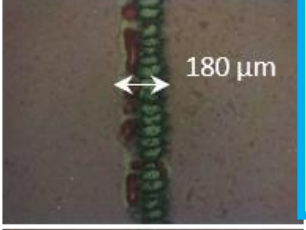



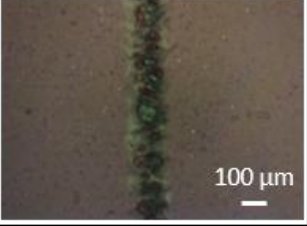
### 3.2. CPBLS process on Cu-doped HA thin films

The Cu-doped HA film prepared from dip-coating were characterized from electronic microscopy. Cross-sections views (SEM) of the 3 final films obtained using 2, 6 and 12 successive coatings (**Figure 3a**) have been realized in order to determine their thickness. Thickness evolution versus the number of successive coatings is plotted (**Figure 3b**). Thin films 5, 13 and 30  $\mu\text{m}$  thick are thus obtained. The increase of film thickness is proportional to the number of successive deposits (linear evolution).



**Figure 3.** SEM cross section views of Cu-doped HA thin films issued for 2, 6 and 12 successive layer coatings and their associated thickness

First, the optimum process CPBLS parameters for each of the three thin films are determined. 0.5 cm long beads (laser lines) at different laser powers and scanning speeds are performed. Powers of 40, 60 and 80 W are studied as well as scanning speeds ranging from 10 up to 250 mm.s<sup>-1</sup>. The optical microscopy images of the CPBLS beads, for the films with an intermediate thickness of 13 μm, are shown in **Figure 4**. The change in colour of the film surfaces from a strong violet coloration to a lighter coloration (desaturated) attests to the passage of the laser. This change in colour has been attributed to a higher light scattering coefficient of the irradiated areas, which can be caused by a change in the surface roughness of the films or in the size of the pores (scattering centres) during laser sintering.

Scanning speed (mm/s)	Power (W)		
	40	60	80
10			
50			
100			
250			

**Figure 4.** Optical microscope images on the film surfaces after CPBLS process using different set of laser parameters. The two images framed in blue are from two films submitted to a same laser linear energy.

Among the parameters used, the power-speed pair of parameters for which a “continuous” laser line is observed, i.e. minimizing the delamination, melting or cracking phenomena, is the one combining the highest speed and the lowest power, that is to say for the lowest linear energy: 40 W - 250 mm.s<sup>-1</sup> (linear energy  $E = 0.16 \text{ J}\cdot\text{mm}^{-1}$ ). The application of higher energy causes the central area of the bead to melt, starting to reveal a vitreous phase in its centre. Another very interesting lesson is that the process performed using the same linear energy but with a couple of different speed - power parameters (couples 40 W – 50 mm.s<sup>-1</sup> and 80 W - 100 mm.s<sup>-1</sup>) leads to different results, in particular the width of the material line

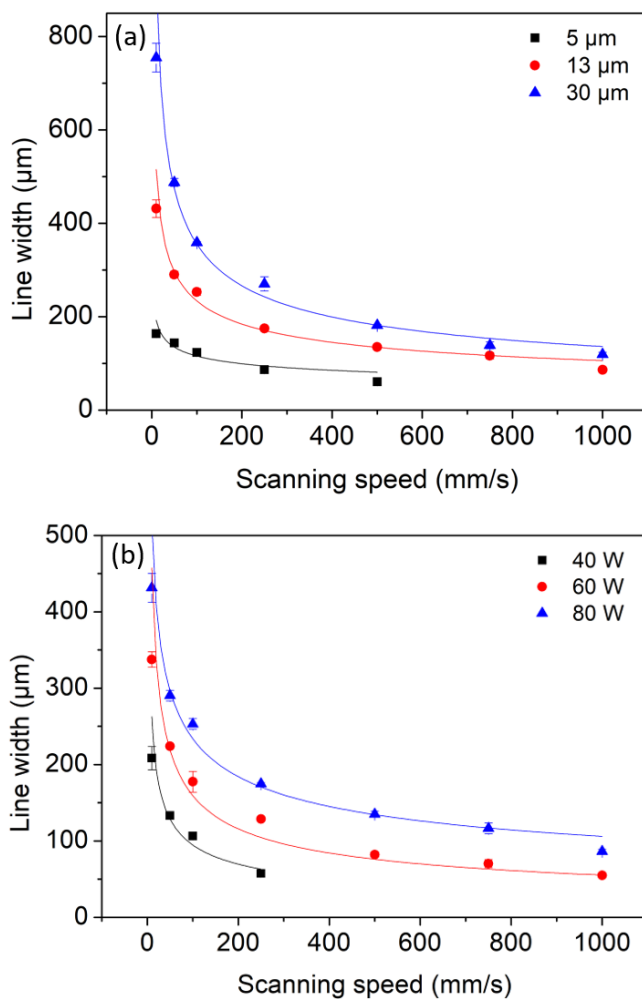


marked by the laser can be changed drastically. Thus, the linear energy received from the laser by the Cu-doped HA film does not appear to be a sufficient parameter to be fully discriminating (relevant) and therefore cannot be the only one to be taken into account with a view to optimizing the process. The two laser parameters: laser speed and laser power have to be studied separately.

Comparing the three films prepared with different thicknesses (5, 13 and 30  $\mu\text{m}$ ), the width of the detectable lased line well depends on both the following three parameters: the scanning speed, the laser power and the film thickness. To illustrate the problematic complexity, the observed lased line width was thus plotted as a function of the scanning speed for the three different film thicknesses at a power of 60 W (**Figure 5a**) and as a function of the scanning speed for the three experimented laser powers on films with the intermediate thickness (13  $\mu\text{m}$  thick) (**Figure 5b**). Line widths were averaged from 5 measurements taken on a single line. The line width evolution curve obeys a power law of the form  $y = a \times x^b$  (with  $a > 300$  and  $b < 0$ ) associated to a very large and sudden increase of width below a "critical" speed of approximately 50-100  $\mu\text{m}$ . One can note that with the aim to produce dense parts by CPBLS, optimal conditions are reached while partial overlap takes place between the successive lased lines. The extreme sensitivity of the lased line width to the different parameters (laser speed, laser power, film thickness) forces the operator to adapt the line interspace for each single set of parameters. Also, very interestingly, the intensity of the impact of the film thickness on the CPBLS effects is about the same order of magnitude than the one of the laser power. It can be posed that the film thickness is linked to the lased line width when the film thickness is lower than the shape of the potential heated volume in depth, limiting hence the efficient laser power transferred to the HA material (substrate no absorbs laser wavelength). So it can be deduced from these experiments that from the possibility to

well control the film thickness using dip-coating process, a focus on the impact of the film thickness has to be managed.

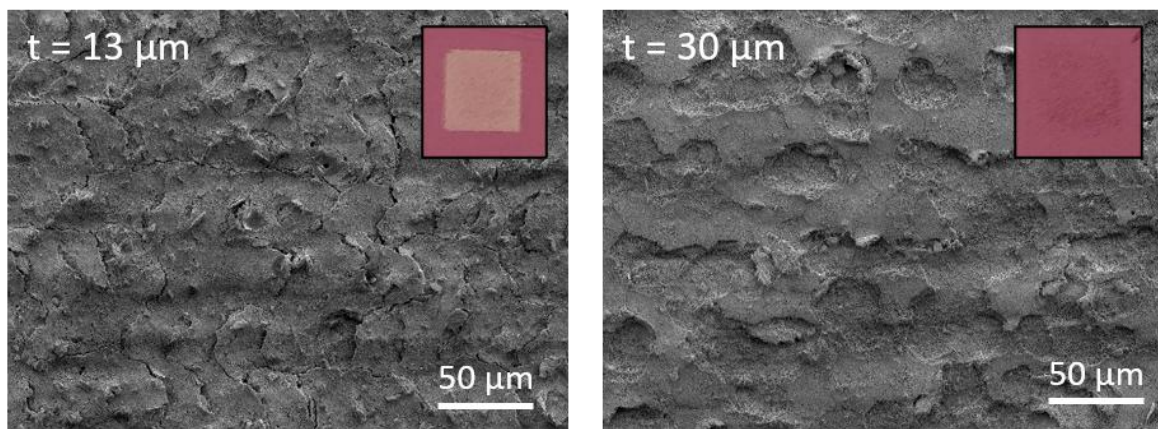
These results show the importance of the Cu-doped HA film thickness on the sintering reaction advancement. In the next step, it was decided to “draw” square-shaped patterns from successive and contiguous lased lines, *i.e.* using for each single set of parameters a hatching space (*hs*) between two successive lines adjusted to the width of the line previously determined, in order to avoid areas undergoing "double" heating.



**Figure 5.** Lased line width evolution versus the laser scanning speed for a fixed laser powder value: 60 W (a) or for a fixed film thickness: 13 μm (b).

Square-shaped patterns by succession of parallel and adjacent laser lines are thus produced at a power of 40 W. Firstly, two laser tests to design sintered square patterns, for the

films which are 13 and 30  $\mu\text{m}$  thick, were carried out respectively at a speed of 250 and 750  $\text{mm}\cdot\text{s}^{-1}$  and with a spacing between the beads of 60 and 40  $\mu\text{m}$ , respectively. The SEM images of the square patterns (sintered areas) confirm the previous optical microscopy results obtained on films submitted to the sintering along a single lased line, namely that the irradiation of the material by the laser causes formation of delaminated chips of material superficial parts (**Figure 6**). For films of such thicknesses, sintering a two-dimensional pattern, as expected, does not solve the chipping problem.

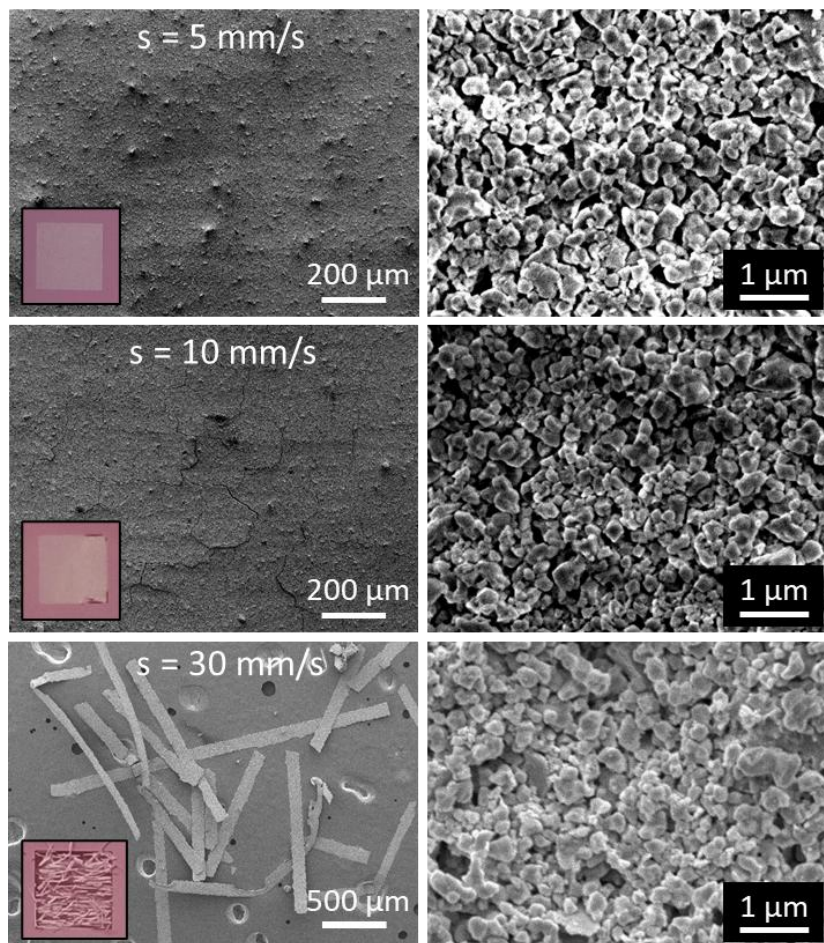


**Figure 6.** SEM micrographs (top view) of square patterns drawn from laser irradiation on thick films (for the film with thickness = 13  $\mu\text{m}$ , the laser parameters are fixed such as  $v = 250 \text{ mm}\cdot\text{s}^{-1}$ ,  $hs = 60 \mu\text{m}$  and for the film with thickness = 30  $\mu\text{m}$ ,  $v = 750 \text{ mm}\cdot\text{s}^{-1}$ ,  $hs = 40 \mu\text{m}$ )

For a 5  $\mu\text{m}$  thick film, *i.e.* the film leading to the most original and interesting results, the SL was carried out at speeds of 5, 10 and 30  $\text{mm}\cdot\text{s}^{-1}$ , at a power of 40 W. The hatching space between the laser lines was set at 80  $\mu\text{m}$  regardless of the scanning speed, as this width remains roughly around 80  $\mu\text{m}$  over this speed range.

For speeds of 5 and 10  $\text{mm}\cdot\text{s}^{-1}$ , continuous square patterns of white coloring compared to the non-lased parts of the film are observed whereas threads (ribbons) form and peel off the substrate using laser scanning speed equal to 30  $\text{mm}\cdot\text{s}^{-1}$  (**Figure 7**). SEM images were taken on each of the samples as well as on a non-sintered zone. At minimum speed, the layer is uniform, no melting or cracking phenomenon is observed while at a speed of 10  $\text{mm}\cdot\text{s}^{-1}$ ,

cracks begin to appear to finally form ribbons corresponding to each laser line at a speed of  $30 \text{ mm}\cdot\text{s}^{-1}$ . Irradiating the material at a very low rate could thus help to attenuate the thermal gradient and promote more diffuse stress relaxation along the lased line. On the contrary, despite a lower linear energy, laser sintering for higher scanning speed induces thermal gradients and therefore greater stresses, and causes the separation of each lased parts (with ribbon shapes) independently of each other.



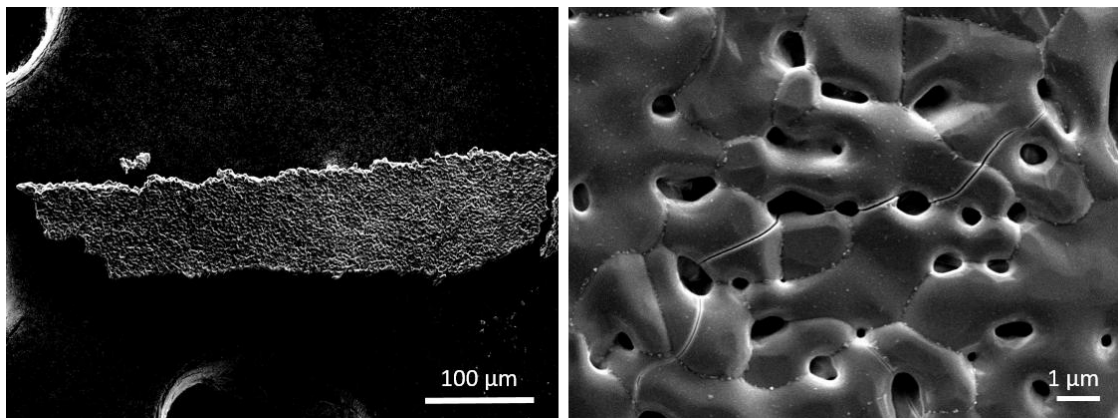
**Figure 7.** SEM micrographs (top view) of square patterns drawn from laser irradiation on the film with thickness =  $5 \mu\text{m}$ , modifying the laser scanning speed between 5 and  $30 \text{ mm}\cdot\text{s}^{-1}$ .

The mechanical cohesion of the ribbons obtained at a speed of  $30 \text{ mm}\cdot\text{s}^{-1}$  (these ribbons are easily handled after their separation) suggests that the sintered areas (square patterns) at lower speed (therefore at higher energy) also have acquired a certain mechanical cohesion. Indeed, the thermal gradients could be minimized for these low speeds, allowing a

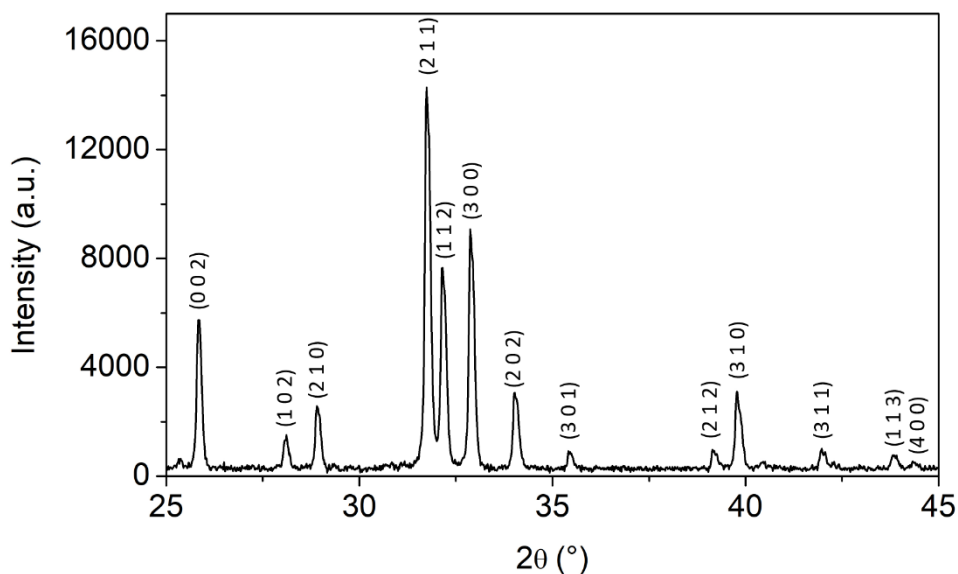
reorganization of the sintered material without micro-cracking. Using these low laser scanning speeds, the energy received by the material being greater, the average temperatures reached during the lasing can be higher. The progress of the sintering is therefore greater at low speeds. Nevertheless, the SEM images at high magnifications do not reflect a progress in the sintering visible for the lased areas compared to the unlased-lased areas: absence of clearly identified sintering necks, reduction of porosity. However, the observation of ribbons peeling off for fast scanning speeds, suggests that the irradiation of the material by the laser beam could have allowed the consolidation of the powder bed thanks to the development of necks between the particles corresponding to the first step of the sintering process.

The ribbons obtained at high laser speed were subjected to post-sintering using high temperature treatment. Annealing of the ribbons, which had detached from the substrate during CPBLS, was carried out at 1300°C for 1 h. This additional heat treatment allows the sintering process to continue. Indeed, the SEM images of the annealed ribbons (**Figure 8**) show the formation of visible grain boundaries between the particles and shrinkage in the width of the tape of about 10% is also noted. Also, X-ray diffraction analysis, to check the maintaining of the Cu-doped HA phase during the CPBLS process and the post-annealing sintering was performed. All diffraction peaks are well indexed to the hydroxyapatite form, indicating the pure target phase is maintained (**Figure 9**). The partial densification of the tape materials is due to the drastic thinness of these ribbons: the diameter of each Cu-doped HA grain is nearly equal to the thickness of the ribbon; thus, the densification of such monolayer of grains is difficult. The increase of the ribbon thickness would allow a better densification to be achieved. Herein, the remaining porosity was evaluated at about 7% using the ImageJ software. Some thin microcracks, possibly appearing during laser sintering or handling the ribbons, are also observed on the surface. Thus, on layers of thinner thickness, selective laser sintering makes it possible to ensure mechanical cohesion to the sintered areas. It could then

be advantageously followed by a natural sintering step, which would strengthen the part shaped and pre-sintered by CPBLS.



**Figure 8.** SEM micrographs of one Cu-doped HA ribbon obtained from CPBLS on the 5  $\mu\text{m}$  thick film using a scanning speed equal to  $30 \text{ mm}\cdot\text{s}^{-1}$  and after post-annealing treatment at  $1300^\circ\text{C}$  during 1 hour.

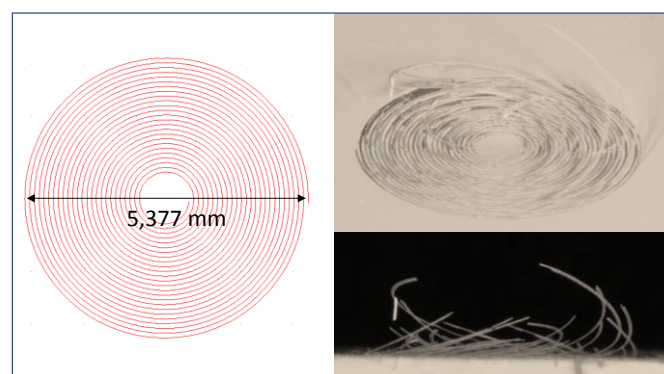


**Figure 9.** X-ray diffraction pattern recorded on a set of consolidated ribbons from the post-annealing treatment at  $1300^\circ\text{C}$  (the peak's indexation considering hydroxyapatite crystallographic network, with space group  $P6_3/m$  space group is joined).

Irradiation of the material at a very slow rate allows the formation of necks between the particles and minimizes the thermal gradient along the bead thus preventing cracking of the powder bed.

Reducing the thickness of the films leads to better behavior under laser irradiation. This should rather come from a decrease in the energy received by the film (due to a film thickness then less than the depth of penetration of the electromagnetic radiation) than from an increase in the elastic properties of the film. This lowering of the received energy allowed us to explore much lower scanning speeds, a key parameter to allow the relaxation of the stresses generated by the start of sintering created under laser. As a result, the production of a pre-sintered film by CPBLS, without cracking phenomenon, was demonstrated on thin film with 5  $\mu\text{m}$  thickness at a power of 40 W and a speed of 5  $\text{mm}\cdot\text{s}^{-1}$  ( $h_s = 80 \mu\text{m}$ )

Moreover, we have shown that the CPBLS technique could allow the creation of self-supported ribbons (with 5  $\mu\text{m}$  thickness, 100  $\mu\text{m}$  width and few mm length) easy to manipulate and which can be post-sintered thanks to the mechanical strength conferred by the neck well visible between grains produced during the CPBLS process. Only ribbons with a width of around one hundred  $\mu\text{m}$  and a thickness of 5  $\mu\text{m}$  have been produced here but, with a light adaptation of the protocol, lasing self-supporting ribbons of more complex geometry can be manufactured as shown in the **Figure 10**.



**Figure 10.** Illustration of a radial pattern ribbon nest obtained with laser scanning speed of 220  $\text{mm}\cdot\text{s}^{-1}$  and laser power of 40 W on a 10  $\mu\text{m}$  thick Cu-doped HAP film.

#### 4. Conclusion

This paper showed deep and transversal work from the powder synthesis to the ceramic shaping thanks to an original direct selective laser sintering process on copper-doped hydroxyapatite (Cu-doped HA) thin films. Cu-doped HA material was investigated because of its potentiality to be used as bone substitute with angiogenic properties enhanced from copper insertion. Furthermore, copper, as chromophore cation absorbing partly the laser wavelength allows heating from laser irradiation.

HA powder was obtained from co-precipitation process mixing calcium and phosphate precursors at a controlled pH. Then, CuO – HA mixtures were submitted to optimized attrition step before a calcination at 1100°C allowing the obtaining of a violet-colored Cu-doped HA powder, monophasic and with sub-micron crystallite size. This powder was formulated to obtain suspension ready to be dip-coated on glass substrates to obtain thin layers with tunable thickness from the number of successive coatings.

Selective Laser Sintering process, was performed on Cu-doped HA layers with different thickness, varying the laser power, the laser scanning speed and the interspace between two lased lines. The success of the ceramic laser sintering: presence or absence of cracks, delamination, mechanical consolidation of the films, but also the control of the lased area (lased line width especially) is shown to strongly depend on the appropriateness of the setting process parameters. As brand new result in regard of the few former studies on ceramic powder laser sintering in literature, it has been shown that the creation of self-supported ribbons (few mm thick and few mm length) can be easily produced. These ribbons are flexible and rollable and can also be post-sintered at high temperatures (1300°C) to be consolidated (hardened). These last experiments, which can be extended to other refractory ionic compounds, open a new window in different ceramic applications: for instance, winding these as-prepared ceramic threads as source of flexible HA ceramic for biomedical



application. Also, for the ceramic film remaining on the substrate, the possibility of taking off patterns of accurate shapes created, “tailor made”, from the additional manufacturing software, can prove to be a more than interesting alternative to lithography.

### **Declaration of competing interest**

The authors declare that they have no known competing financial interests or personal relationships that could have appeared to influence the work reported in this paper.

### **Acknowledgements**

The authors thank to the French regional council of Nouvelle Aquitaine for the financial funding given to this study. This work was also supported by institutional grants from the National Research Agency under the Investments for the future program with the reference ANR-10-LABX-0074-01 Sigma-LIM.

### **References**

- [1] T. Chartier, C. Dupas, M. Lasgorceix, J. Brie, E. Champion, N. Delhote, Ch. Chaput, Additive Manufacturing to Produce Complex 3D Ceramic Parts, *J. Ceram. Sci. Tech.*06 (2014) 95-104. <https://doi.org/10.4416/JCST2014-00040>.
- [2] Y. Chen, T. Li, Z. Jia, F. Scarpa, C.-W. Yao, L. Wang, 3D printed hierarchical honeycombs with shape integrity under large compressive deformations, *Mater. Des.*137 (2018) 226-234. <https://doi.org/10.1016/j.matdes.2017.10.028>.
- [3] I. Yadroitsev, P. Krakhmalev, I. Yadroitsava, Hierarchical design principles of selective laser melting for high quality metallic objects, *Addit. Manuf.*7 (2015) 45-56. <https://doi.org/10.1016/j.addma.2014.12.007>.

- [4] R. Leal, F.M. Barreiros, L. Alves, F. Romeiro, J. C. Vasco, M. Santos, C. Marto, Additive manufacturing tooling for the automotive industry, *Int. J. Adv. Manuf. Technol.*92 (2017) 1671-1676, <https://doi.org/10.1007/s00170-017-0239-8>.
- [5] R. Liu, Z. Wang, T. Sparks, F. Liou, J. Newkirk, Aerospace applications of laser additive manufacturing, in: M. Brandt (Eds.), *Laser Additive Manufacturing*, Woodhead Publishing, 2017, pp. 351-371.
- [6] L. S. Dimas, G. H. Bratzel, I. Eylon, M. J. Buehler, Tough Composites Inspired by Mineralized Natural Materials: Computation, 3D printing, and Testing, *Adv. Funct. Mater.*23 (2013) 4629-4638. <https://doi.org/10.1002/adfm.201300215>.
- [7] F. Ning, W. Cong, J. Qiu, J. Wei, S. Wang, Additive manufacturing of carbon fiber reinforced thermoplastic composites using fused deposition modeling, *Compos. Part B Eng.*80 (2015) 369-378, <https://doi.org/10.1016/j.compositesb.2015.06.013>.
- [8] F. Rengier, A. Mehndiratta, H. von Tengg-Kobligk, C. M. Zechmann, R. Unterhinninghofen, H.-U. Kauczor, F. L. Giesel, 3D printing based on imaging data: review of medical applications, *Int. J. Comput. Assist. Radiol. Surg.*5 (2010) 335-341. <https://doi.org/10.1007/s11548-010-0476-x>.
- [9] N. K. Vail, L. D. Swain, W. C. Fox, T. B. Aufdemorte, G. Lee, J. W. Barlow, Materials for biomedical applications, *Mater. Des.*20 (1999) 123-132. [https://doi.org/10.1016/S0261-3069\(99\)00018-7](https://doi.org/10.1016/S0261-3069(99)00018-7).
- [10] F. Edith Wiria, N. Sudarmadji, K. Fai Leong, C. Kai Chua, E. Wei Chng, C. Chai Chan, Selective laser sintering adaptation tools for cost effective fabrication of biomedical prototypes, *Rapid Prototyp. J.*16, (2010) 90-99, <https://do.org/10.1108/13552541011025816>.
- [11] B. Duan, M. Wang, Selective laser sintering and its application in biomedical engineering, *MRS Bull.*36 (2011) 998-1005. <https://doi.org/10.1557/mrs.2011.270>.

- [12] A. Mazzoli, Selective laser sintering in biomedical engineering, *Med. Biol. Eng. Comput.*51 (2013) 245-256. <https://doi.org/10.1007/s11517-012-1001-x>.
- [13] S. F. S. Shirazi, S. Gharekhani, M. Mehrali, H. Yarmand, H. S. Cornelis Metselaar, N. A. Kadri, N. A. A. Osman, A review on powder-based additive manufacturing for tissue engineering: selective laser sintering and inkjet 3D printing, *Sci. Technol. Adv. Mater.*16 (2015) e-033502. <https://doi.org/10.1088/1468-6996/16/3/033502>.
- [14] E. Champion, A. Magnaudeix, P. Pascaud-Mathieu, T. Chartier, Advanced processing techniques for customized ceramic medical devices, in: Paola Palmero, Francis Cambier and Eamonn De Barra (Eds.), *Advances in Ceramic Biomaterials*, 2017, pp. 433-468.
- [15] H. N. Chia, B. M. Wu, Recent advances in 3D printing of biomaterials, *J. Biol. Eng.*9 (2015) e-4. <https://doi.org/10.1186/s13036-015-0001-4>.
- [16] T. Chartier, C. Chaput, F. Doreau, M. Loiseau, Stereolithography of structural complex ceramic parts, *J. Mater. Chem. Sci.*37 (2002) 3141-3147.  
<https://doi.org/10.1023/A:1016102210277>.
- [17] K. H. Tan, C. K. Chua, K. F. Leong, C. M. Cheah, P. Cheang, M. S. Abu Bakar, S. W. Cha, Scaffold development using selective laser sintering of polyetheretherketone–hydroxyapatite biocomposite blends, *Biomater.*24 (2003) 3115-3123.  
[https://doi.org/10.1016/S0142-9612\(03\)00131-5](https://doi.org/10.1016/S0142-9612(03)00131-5).
- [18] Y. Zhang, L. Hao, M. M. Savalani, R. A. Harris, L. Di Silvio, K. E. Tanner, In vitro biocompatibility of hydroxyapatite-reinforced polymeric composites manufactured by selective laser sintering, *J. Biomed. Mater. Res.*91A (2009) 1018-1027.  
<https://doi.org/10.1002/jbm.a.32298>.
- [19] T. Kumaresan, R. Gandhinathan, M. Ramu, M. Ananthasubramanian, K. B. Pradheepa, Design, analysis and fabrication of polyamide/ hydroxyapatite porous structured scaffold

using selective laser sintering method for bio-medical applications, *J. Mech. Sci. Technol.*30 (2016) 5305-5312. <https://doi.org/10.1007/s12206-016-1049-x>.

[20] F. Dabbas, S. L. Stares, J. M. Mascheroni, D. Hotza, G. V. Salmoria, Selective Laser Sintering of Polyamide/Hydroxyapatite Scaffolds, in: M. A. Meyers, H. A. C. Benavides, S. P. Brühl, H. A. Colorado, E. Dalgaard, C. N. Elias, R. B. Figueiredo, O. Garcia-Rincon, M. Kawasaki, T. G. Langdon, R. V. Mangalaraja, M. C. G. Marroquin, A. da Cunha Rocha, J. M. Schoenung, A. Costa e Silva, M. Wells, W. Yang (Eds), *Proc. 3<sup>rd</sup> Pan American Materials Congress*, 2017, pp. 95-103.

[21] J. M. Williams, A. Adewunmi, R. M. Schek, C. L. Flanagan, P. H. Krebsbach, S. E. Feinberg, S. J. Hollister, S. Daset, Bone tissue engineering using polycaprolactone scaffolds fabricated via selective laser sintering, *Biomater.*26 (2005) 4817-4827.  
<https://doi.org/10.1016/j.biomaterials.2004.11.057>.

[22] S. Eosoly, D. Brabazon, S. Lohfeld, L. Looney, Selective laser sintering of hydroxyapatite/poly- $\epsilon$ -caprolactone scaffolds, *Acta Biomater.*6 (2010) 2511-2517.  
<https://doi.org/10.1016/j.actbio.2009.07.018>.

[23] C. Shuai, P. Feng, C. Cao, S. Peng, Processing and characterization of laser sintered hydroxyapatite scaffold for tissue engineering, *Biotechnol. Bioprocess Eng.*18 (2013) 520-527. <https://doi.org/10.1007/s12257-012-0508-1>.

[24] C. Shuai, Y. Nie, C. Gao, P. Feng, J. Zhuang, Y. Zhou, S. Peng, The microstructure evolution of nanohydroxapatite powder sintered for bone tissue engineering, *J. Exp. Nanosci.*8 (2013) 762-773. <https://doi.org/10.1080/17458080.2011.606507>.

[25] A. Simchi, Direct laser sintering of metal powders: Mechanism, kinetics and microstructural features, *Mater. Sci. Eng. A* 428 (2006) 148-158.  
<https://doi.org/10.1016/j.msea.2006.04.117>.

- [26] F. L. Amorim, A. Lohrengel, V. Neubert, C. F. Higa, T. Czelusniak, Selective laser sintering of Mo-CuNi composite to be used as EDM electrode, *Rapid Prototyp. J.*20 (2014) 59-68. <https://doi.org/10.1108/RPJ-04-2012-0035>.
- [27] D. Gu et Y. Shen, « Effects of processing parameters on consolidation and microstructure of W–Cu components by DMLS », *J. Alloys Compd.*, vol. 473, no 1-2, p. 107-115, avr. 2009, doi: 10.1016/j.jallcom.2008.05.065.
- [28] S. Meyers, J.-P. Kruth, J. Vleugels, Direct selective laser sintering of reaction bonded silicon carbide, *Solid Freeform Fabrication Symposium Proceedings*, 2015, 1750 - 1758.
- [29] K. G. Prashanth, S. Scudino, T. Maity, J. Das, J. Eckert, Is the energy density a reliable parameter for materials synthesis by selective laser melting?, *Mater. Res. Lett.*5 (2017) 386-390. <https://doi.org/10.1080/21663831.2017.1299808>.
- [30] P. K. Subramanian, J. W. Barlow, H. L. Marcus, Selective laser sintering of alumina with polymer binders, *Rapid Prototyp. J.*1 (1995) 24–35. <https://doi.org/10.1108/13552549510086844>.
- [31] Y.-A. Song, W. Koenig, Experimental Study of the Basic Process Mechanism for Direct Selective Laser Sintering of Low-Melting Metallic Powder, *CIRP Ann.*46 (1997) 127-130. [https://doi.org/10.1016/S0007-8506\(07\)60790-2](https://doi.org/10.1016/S0007-8506(07)60790-2).
- [32] Y. Tang, J. Y. H. Fuh, H. T. Loh, Y. S. Wong, L. Lu, Direct laser sintering of a silica sand, *Mater. Des.*24 (2003) 623-629. [https://doi.org/10.1016/S0261-3069\(03\)00126-2](https://doi.org/10.1016/S0261-3069(03)00126-2).
- [33] J.-P. Kruth, P. Mercelis, J. Van Vaerenbergh, L. Froyen, M. Rombouts, Binding mechanisms in selective laser sintering and selective laser melting, *Rapid Prototyp. J.*11 (2005) 26-36. <https://doi.org/10.1108/13552540510573365>.
- [34] Y. Tang, J. Y. H. Fuh, H. T. Loh, Y. S. Wong, L. Lu, Direct laser sintering of a silica sand, *Mater. Des.*24 (2003) 623-629. [https://doi.org/10.1016/S0261-3069\(03\)00126-2](https://doi.org/10.1016/S0261-3069(03)00126-2).

- [35] Y. Tang, H. T. Loh, Y. S. Wong, J. Y. H. Fuh, L. Lu, X. Wang, Direct laser sintering of a copper-based alloy for creating three-dimensional metal parts, *J. Mater. Process. Technol.*140 (2003) 368-372. [https://doi.org/10.1016/S0924-0136\(03\)00766-0](https://doi.org/10.1016/S0924-0136(03)00766-0).
- [36] S. Kumar, Selective Laser Sintering/Melting, in: M. S.J.Hasmi (Eds), *Comprehensive Materials Processing*, Elsevier, 2014, p. 93-134.
- [37] E. Juste, F. Petit, V. Lardot, F. Cambier, Shaping of ceramic parts by selective laser melting of powder bed, *J. Mater. Res.*29 (2014) 2086-2094.  
<https://doi.org/10.1557/jmr.2014.127>.
- [38] T. Bazin, Synthèse, caractérisations structurales par spectroscopies et mise en forme d'hydroxyapatites dopées au cuivre ou au fer, PhD manuscript, Université de Limoges / Université de Bordeaux, 2020. <http://www.theses.fr/2020BORD0118>.
- [39] S. Raynaud, Synthèse, frottage et propriétés mécaniques de phosphates de calcium dans le système hydroxyapatite – phosphate tricalcique, PhD manuscript, Université de Limoges, 1999, <http://www.theses.fr/1999LIMO0035>
- [40] T. Bazin, A. Magnaudeix, R. Mayet, P. Carles, I. Julien, A. Demourgues, M. Gaudon, E. Champion, Sintering and biocompatibility of copper-doped hydroxyapatite bioceramics, *Ceram. Int.* (2021) In Press, <https://doi.org/10.1016/j.ceramint.2021.01.225>
- [41] L. Ferrage, G. Bertrand, P. Lenormand, Dense yttria-stabilized zirconia obtained by direct selective laser sintering, *Addit. Manuf.*21 (2018) 472-478.  
<https://doi.org/10.1016/j.addma.2018.02.005>.